

Imaging lattice reconstruction in homobilayers and heterobilayers of transition metal dichalcogenides

Anna Rupp,¹ Jonas Göser,¹ Zhijie Li,¹ Ismail Bilgin,¹ Anvar Baimuratov,¹ and Alexander Högele^{1,2}

¹*Fakultät für Physik, Munich Quantum Center (MQC), and Center for NanoScience (CeNS), Ludwig-Maximilians-Universität München, Geschwister-Scholl-Platz 1, 80539 München, Germany*

²*Munich Center for Quantum Science and Technology (MCQST), Schellingtr. 4, 80799 München, Germany*
(Dated: June 27, 2023)

Moiré interference effects have profound impact on the optoelectronic properties of vertical van der Waals structures. Here we establish secondary electron imaging in a scanning electron microscope as a powerful technique for visualizing registry-specific domains in vertical bilayers of transition metal dichalcogenides with common moiré phenomena. With optimal parameters for contrast-maximizing imaging of high-symmetry registries, we identify distinct crystal realizations of WSe₂ homobilayers and MoSe₂-WSe₂ heterobilayers synthesized by chemical vapor deposition, and demonstrate ubiquitous lattice reconstruction in stacking-assembled bilayers with near parallel and antiparallel alignment. Our results have immediate implications for the optical properties of registry-specific excitons in layered stacks of transition metal dichalcogenides, and demonstrate the general potential of secondary electron imaging for van der Waals twistrionics.

Interference effects in vertical stacks of twisted two-dimensional crystal lattices induce moiré patterns, with rich consequences for charge carrier transport in the emergent mini-bands of the electronic band structure. As such, moiré effects give rise to peculiar transport phenomena in twisted homobilayer stacks of transition metal dichalcogenides (TMDs) [1–3] and also strongly affect the optoelectronic properties of TMD heterobilayers [4–7] with phenomena ranging from moiré intralayer [8–11] and interlayer [8, 11–16] excitons or hybrid excitons [17–20]. The actual manifestation of transport and optical phenomena depends in leading order on the twist angle and lattice mismatch, but additional effects of lattice reconstruction can be quite substantial [11, 21–31]. Ultimately, the details of moiré lattices and their reconstruction are essential for the interpretation of observed phenomena.

Established imaging techniques with required resolution include conductive atomic force microscopy [22, 24], scanning tunneling microscopy [28, 29, 32], scanning transmission electron microscopy [24, 32] and dark-field transmission electron microscopy [22, 33]. Providing high spatial resolution down to the limit of single atoms often involves extensive sample preparation methods. In contrast, scanning electron microscopy (SEM) combines comparably high spatial resolution with simple sample preparation. Moreover, SEM can provide complementary information such as elemental layer composition [34] or crystallographic orientation [35] in secondary electron imaging, revealing reconstruction patterns in WSe₂ homobilayers with near-parallel alignment [27].

In the following, we demonstrate the adoption and optimization of secondary electron imaging in a standard SEM for the visualization of domains with distinct atomic registries emerging in vertical TMD bilayers due to lattice reconstruction. To this end, we fabricate on the one hand TMD homobilayers and heterobilayers by stamping-assemblies of monolayers obtained from chemical vapor deposition (CVD), and on the other hand CVD-grown vertical homo- and heterobilayers, each with parallel and antiparallel alignment. With optimized operation conditions and numerical simulations, we

identify domains of different atomic registries by their contrast in secondary electron imaging. We observe characteristic features of mesoscopic reconstruction, and find two distinct realizations of stable registries for parallel bilayer stacks grown directly by CVD-synthesis.

In ideal moiré superlattices formed by two hexagonal lattices upon vertical stacking with finite twist or lattice mismatch as indicated schematically in Fig. 1(a), the characteristic moiré superlattice constant is given by $L_M(\delta) = a_1/\sqrt{1 + (a_1/a_2)^2 - 2(a_1/a_2)\cos\delta}$, with the lattice constants of the two layers a_1 and a_2 , and the relative twist angle δ (modulo 60°) [36]. Within one moiré supercell, three high-symmetry atomic registries stand out, illustrated by colored circles in Fig. 1(b) - for heterobilayer stacks of non-centrosymmetric TMD monolayers: H_h^M , H_h^h as well as H_h^X , and R_h^M , R_h^h as well as R_h^X stackings for near antiparallel (H-type) and parallel (R-type) alignment, respectively. The superscript and subscript refer to the electron and hole layer respectively, with M, X, and h denoting the transition metal atom, the chalcogen atom, and the hexagon center [8, 37].

In the rigid-lattice moiré limit, all three stackings recur upon lateral translation as in the left halves of the bottom circles in Fig. 1(b) for both H- and R-type stacks. In non-rigid bilayers which allow for finite atom displacement, however, the areas of energetically favorable H_h^h , R_h^M and R_h^X atomic registries are maximized at the expense of other stackings to give rise to periodically reconstructed patterns [21] that differ for H- and R-type stacks shown in the right halves of the bottom circles in Fig. 1(b), respectively. In theory, periodic reconstruction yields hexagonal H_h^h domains in H-type and alternating triangular R_h^M and R_h^X domains in R-type stacks [21, 23, 30], with domain sizes proportional to the moiré period length L_M ranging from a few to a few tens of nanometers. In practice, however, regions of regular periodic reconstruction are rather limited, and irregular reconstructed landscapes with variations on mesoscopic length scales prevail instead [11, 22, 24–29, 31].

Secondary electron detection in SEM represents a powerful experimental method to visualize reconstructed crystal mor-

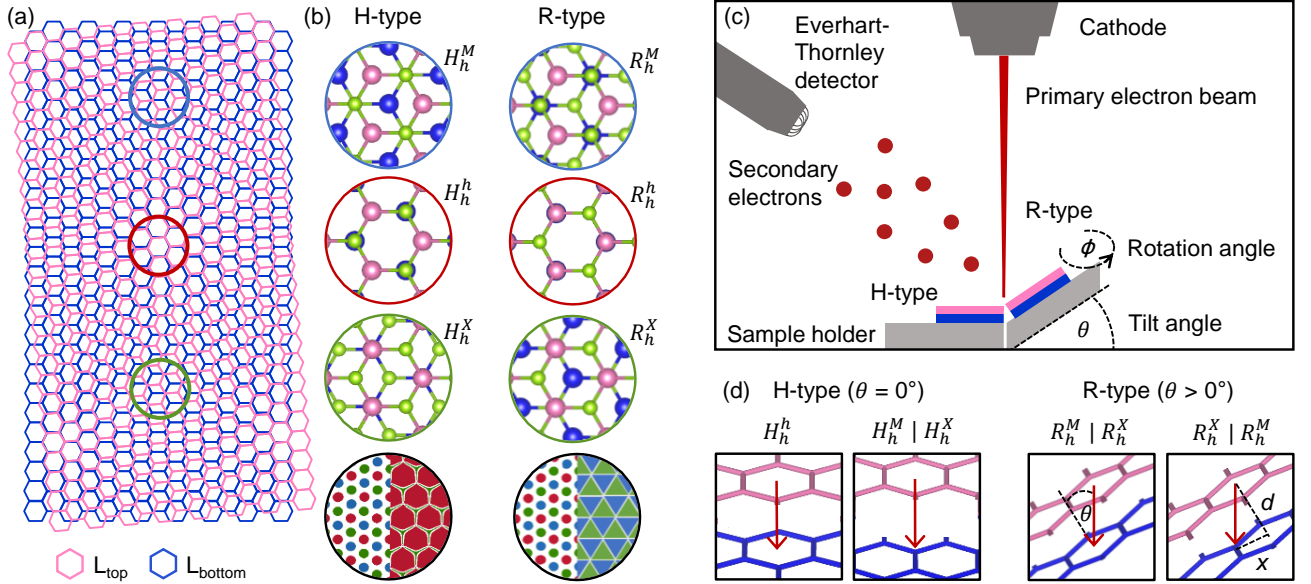


FIG. 1. (a) Schematics of moiré interference pattern in twisted bilayers, with points of three high-symmetry stackings indicated by colored circles. (b) Left (right) panel: Top view of the corresponding high-symmetry stackings H_h^M , H_h^h and H_h^X (R_h^M , R_h^h and R_h^X) in antiparallel H-type bilayer (parallel R-type bilayer). The schematics in the bottom panel illustrate the rigid-lattice moiré pattern in the left halves of the circles which transforms upon reconstruction into hexagonal H_h^h domains (triangular R_h^M and R_h^X domains) shown in the right halves. (c) Principle of reconstruction pattern imaging with a scanning electron microscope (not to scale): interactions between primary electrons and bilayer stack give rise to secondary electron emission detected with an Everhart-Thornley detector. The detection yield depends on the packing density of the incoming beam with respect to the bilayer. H-type imaging is performed at normal incidence, whereas R-type imaging requires a sample tilt θ and rotation angle ϕ for optimal contrast. (d) Side view of H-type imaging: At normal incidence channelling occurs only in the H_h^h stacking. Side view of R-type imaging: Tilting the sample to θ results in channelling for only one stacking.

phology on length scales down to the spatial resolution limit of low-energy primary electrons. It is based on the detection of secondary electrons generated by inelastic scattering of the primary electron beam with core or valence electrons of the sample, with the principle of operation shown in the schematics of Fig. 1(c). Given kinetic energies of secondary electrons below 50 eV, their escape depth is confined to near-surface regions. A conventional Everhart-Thornley detector inside the SEM records the secondary electron yield at each scan position and converts it into a grey value of an image pixel. The more interactions between primary electrons and surface-layer atoms occur, the more secondary electrons are generated and counted, corresponding to a brighter image pixel [38, 39]. Due to distinct stackings, different experimental conditions are required for optimal imaging of H- and R-type bilayers, as indicated in Fig. 1(c) and (d).

To begin with, we consider the concept of optimal channelling conditions for secondary electrons in H- and R-type stacks. For H-type stacks, optimal channelling is realized at normal incidence of the incoming beam (corresponding to a tilt angle $\theta = 0^\circ$), as illustrated in Fig. 1(d). This configuration gives rise to maximum contrast between domains of H_h^h atomic registry and H_h^M or H_h^X domains with higher packing density from the perspective of the incoming beam. The difference in the packing density for normal incidence in turn results in different secondary electron yields and hence different contrast in the SEM image. The intuitive model of classical electrons suggests less interactions between primary elec-

trons and lattice atoms for the channelling condition in the left panel of Fig. 1(d), where the electron trajectory is indicated to pass the hexagon centers of both layers in the H_h^h case as opposed to encountering the hexagon corner of the bottom layer in H_h^M or H_h^X stacking. The wave nature of low-energy electrons, however, leads to diffraction, which in the channelling case gives rise to more backscattering of primary electrons and thus an increased generation of secondary electrons upon reversed propagation of backscattered electron to the surface [40]. Overall, the secondary electron yield is thus higher for the channelling condition [35], and H_h^h domains appear bright in SEM imaging while H_h^M and H_h^X stacks are dark.

Maximum contrast at normal incidence is not expected for bilayers with R-type parallel alignment and reconstruction into R_h^M and R_h^X domains with similar packing densities. In contrast to optimal conditions at normal incidence for H-stacks, a finite tilt of the sample at angle θ is required to obtain channelling with mutually contrasting generation yields of secondary electrons by domains of R_h^M and R_h^X atomic registries, as illustrated in the right panel of Fig. 1(d). Again, channelling results in a higher secondary electron yield and thus a brighter image pixel. The optimal tilt angle can be calculated from the channelling condition shown in Fig. 1(d) as $\theta = \arctan(x/d)$ with the lateral distance of the beam passage through the bilayers x and the vertical interlayer distance d . Moreover, for samples with finite tilt angle θ , the secondary electron yield, and hence the image grey value, is also a function of the rotation angle ϕ . This in turn allows to discriminate

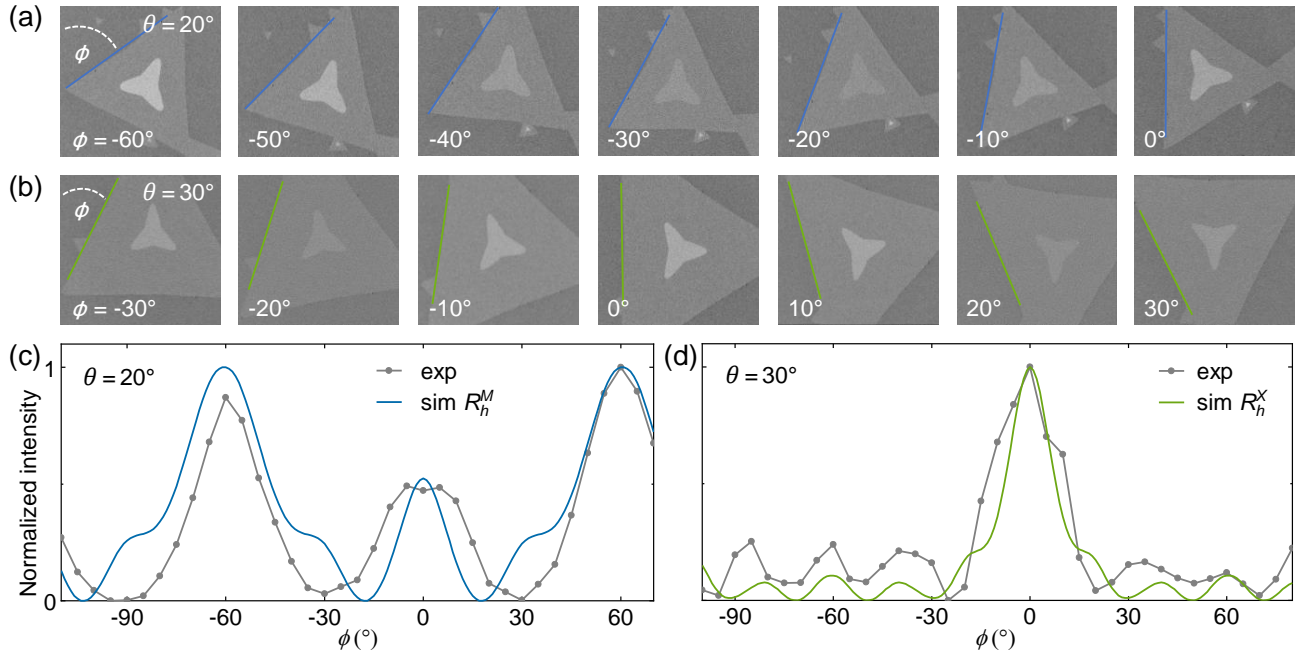


FIG. 2. (a) and (b), Secondary electron images of two CVD-grown R-type WSe_2 homobilayers tilted to $\theta = 20^\circ$ and 30° , respectively, for different values of the rotation angle ϕ in steps of 10° . (c) and (d), Corresponding contrast modulation in experiment (grey data in steps of 5°) and simulations (blue and green solid lines for R_h^M or R_h^X stackings, respectively) as a function of the rotation angle ϕ . Note that the two homobilayers synthesized in the same CVD process differ in their R-type stacking.

between R_h^M and R_h^X stacked domains.

The dependence of the imaging contrast on the tilt and rotation angles, θ and ϕ , are shown in Fig. 2 for CVD-grown WSe_2 homobilayers. The use of CVD-bilayers is particularly advantageous, as the crystallographic orientation is directly evident from the relative ordination of the inner and outer triangular-shaped crystal layers. In Fig. 2(a) and (b), the two R-type bilayers, synthesized in the same growth process, feature parallel alignment of top (bright) and bottom (dark) triangles (with deviations from triangular shapes in the top layer). Both bilayer crystals exhibit contrast modulation in Fig. 2(a) and (b) as a function of rotation angle ϕ for tilt angles $\theta = 20^\circ$ and 30° , respectively. The contrast modulation is cyclic in ϕ (with $\phi = 0^\circ$ defined with respect to the tilt axis chosen collinear with the triangle edge that is closest to the secondary electron detector, and positive values corresponding to counterclockwise rotation), as evident from the normalized data in Fig. 2(c) and (d). At each point, the grey value of the substrate was subtracted from the grey value of the bilayer, and the contrast was normalized to the cyclic maximum.

Even though both bilayers of Fig. 2(a) and (b) are clearly R-type, they exhibit different contrast evolution in secondary electron imaging as a function of θ and ϕ . To identify the respective registry configurations, we performed Monte-Carlo simulations of the secondary electron yield as a function of tilt and rotation angle for all high-symmetry stackings of R- and H-type bilayers [27] (see Methods for details). For R-type, the simulations shown by solid lines in Fig. 2(c) and (d) reproduce the experimental contrast modulations with very good agreement and lead to the following main conclusions. Most gen-

erally, higher tilt angles yield larger contrast modulations due to increasing interaction volume with tilt. Moreover, the contrast modulation under ϕ -rotation, with a periodicity of 120° due to crystal symmetry, is characteristic for a given tilt angle θ and registry, discriminating between R_h^M and R_h^X atomic registries of the homobilayers in Fig. 2. To the best of our knowledge, this observation is the first to identify CVD-grown homobilayers in the contrasting limits of fully reconstructed R_h^M and R_h^X crystal stackings.

This contrasting behavior in secondary electron imaging is highlighted in Fig. 3 on another pair of WSe_2 homobilayer flakes obtained in the same synthesis run. For the same tilt angle of $\theta = 38^\circ$, which represents a balanced optimum between increased modulation contrast and reduced spatial resolution upon tilt, we clearly observe the limiting cases of R_h^M and R_h^X reconstructed domains for the homobilayer crystals in Fig. 3(a) and (b) for the same rotation angles $\phi = 10^\circ, 20^\circ, 30^\circ$ and 40° . Consistently, the respective normalized contrasts in Fig. 3(c) differ substantially for the two registries upon ϕ -rotation, maximizing the registry-discriminating contrast for specific ϕ values ($20^\circ, 40^\circ, 80^\circ$ and 100°).

Equipped with this understanding and optimized operation parameters, we utilized secondary electron imaging to visualize reconstruction effects in stacking-assembled MoSe_2 homobilayers and MoSe_2 - WSe_2 heterobilayers, each near antiparallel and parallel alignment. The samples were fabricated with a stamping-based direct pick up method [41] by placing a CVD-grown monolayer onto another monolayer CVD-grown on a Si/SiO_2 substrate. The relative orientation close to 0° or 180° alignment was again facilitated by the triangular shapes

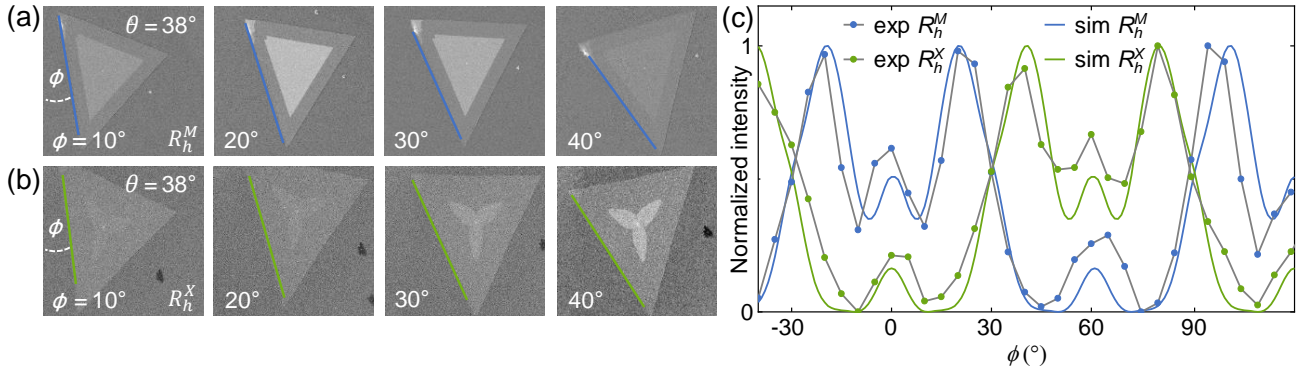


FIG. 3. (a) and (b), SEM images of two CVD-grown R-type WSe₂ bilayers both tilted to $\theta = 38^\circ$ and inspected at the same ϕ -angles. The reversed contrast indicates opposite stacking orders. The corresponding contrast modulations for both bilayers as a function of the rotation angle are shown by the grey lines in (c). Simulations of R_h^M and R_h^X WSe₂ bilayers for $\theta = 38^\circ$ tilt as a function of the rotation angle assign the R_h^M and R_h^X stackings to the top and bottom bilayer in (a) and (b), respectively. Owing to the 60° shifted modulation between R_h^M and R_h^X stackings only four angles exhibit maximum contrast between the two stackings.

of monolayer crystals, with an accuracy of $\pm 0.3^\circ$ as determined a posteriori with SEM. Using optimized parameters discussed above, secondary electron imaging was performed at $\theta = 0^\circ$ and 38° for H- and R-type stacks, respectively.

Overall, the morphologies of mechanically stacked homobilayer MoSe₂ in Fig. 4(a) and (b) and heterobilayer MoSe₂-WSe₂ in Fig. 4(c), (d) and (e) are consistent with lattice reconstruction on mesoscopic length scales [11, 22, 24–29, 31]. In secondary electron images of H-type stacks, recorded at zero tilt and shown in Fig. 4(a) and (c), bright regions correspond to H_h^H stacking. The images of R-type stacks in Fig. 4(b), (d) and (e), recorded at $\theta = 38^\circ$ and $\phi = -20^\circ$, exhibit maximum contrast between bright R_h^M and dark R_h^X stackings. All images show local variations in the domain pattern, with relatively large domains frequently found near edges or folds, and rather periodic patterns with domain sizes well below 100 nm observed predominantly in the sample core. In accord with theoretical anticipation of lattice reconstruction from moiré to periodic domains with hexagonal and triangular tiling in H- and R-type stacks [21, 23], we frequently observed domains with the corresponding geometries, as emphasized in the insets of Fig. 4(a), (b) and (c), as well as in Fig. 4(d).

Remarkably, the inspection of R-type homobilayers as in Fig. 4(b) indicates that both bright and dark domains of R_h^M and R_h^X stackings emerge upon large-scale reconstruction [21, 23], whereas heterobilayers tend to reconstruct preferentially into bright R_h^M domains at the expense of dark R_h^X domains as in Fig. 4(d) and (e). This suggests an energetic imbalance in the competition between R_h^M and R_h^X registries in heterobilayers that is absent in homobilayers, in accord with DFT calculations for MoSe₂-WSe₂ heterobilayer with a slightly favored R_h^M stacking [22, 32].

The competition between domains of R_h^M and R_h^X registries in large-scale reconstruction is even more evident in CVD-grown MoSe₂-WSe₂ heterobilayers. In Fig. 5(a), we show optical and secondary electron images of a MoSe₂-WSe₂ heterostack formed by small WSe₂ triangular monolayers on top of a large MoSe₂ monolayer triangle. The zoom

to the secondary electron image at normal incidence ($\theta = 0^\circ$) in Fig. 5(b) singles out a section with three representative triangles encircled in red, green and blue, which we inspected at a tilt of $\theta = 38^\circ$ for two rotation angles ϕ of 25° and 40° in Fig. 5(c) and (d), respectively.

First, we point out similar grey-scale contrasts observed at $\theta = 0^\circ$ for all three triangles in Fig. 5(a) and (b). However, at finite tilt of $\theta = 38^\circ$, they interchange their relative brightness upon rotation from $\phi = 25^\circ$ to 40° in Fig. 5(c) and (d), respectively. This behavior, combined with our understanding of registry-specific contrasts from simulations, identify the triangles marked in red, green and blue as exhibiting complete lattice reconstruction into H_h^h , R_h^X , and R_h^M domains. The mutual exclusion of the latter two, in particular, is a hallmark of the energy-driven competition between two near-optimal stackings in R-type MoSe₂-WSe₂ heterostacks for large-area domains.

The observation of nearly complete reconstruction of CVD-grown WSe₂-MoSe₂ heterobilayers (except for the inner cores as discussed previously elsewhere [32]) into one exclusive registry is remarkable, and was observed as a robust feature on more than 70 heteroflakes. The distribution of distinct stackings for H- and R-type heterostacks is shown in Fig. 5(e), featuring H_h^h as the singular stacking for H-type stacks, and the R_h^M stacking outcompeting the R_h^X stacking with a ratio of ~ 3 . This distribution provides further support into the energetic preference of MoSe₂-WSe₂ with regard to reconstruction into R_h^M domains as predicted by DFT calculations [22, 32].

In summary, we reported secondary electron imaging of reconstructed homo- and heterobilayers, each with parallel and antiparallel alignment. Whereas registry contrast in antiparallel bilayers is readily achieved with low beam energy and high resolution at normal incidence, discrimination of different domains in parallel stacks requires optimization of both tilt and rotational angles. With optimized parameters and numerical simulations, we identified lattice reconstruction on mesoscopic length scales as the predominant effect in the

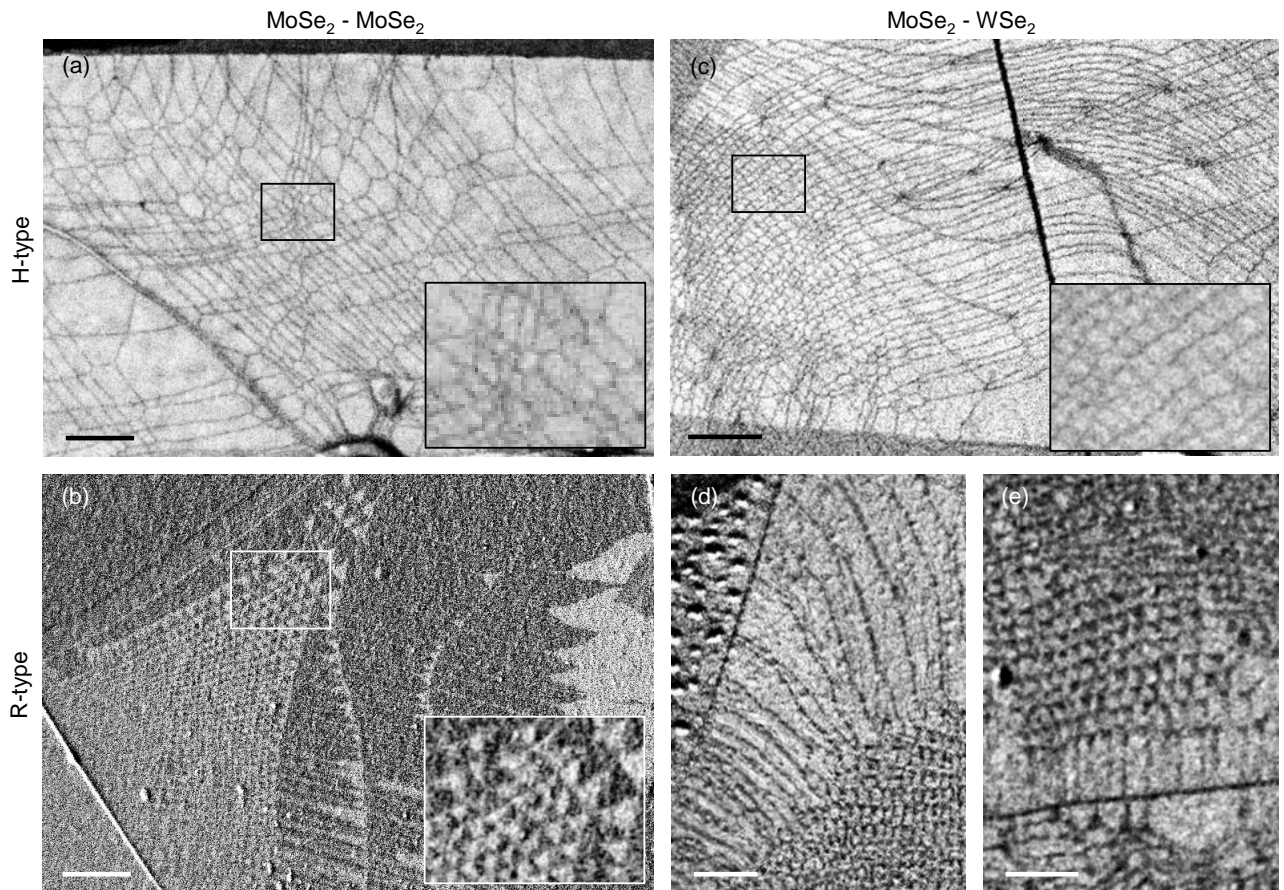


FIG. 4. (a) and (b), Secondary electron images of twisted H-type ($\delta = 179.6^\circ$) and R-type ($\delta = 0.2^\circ$) MoSe₂ homobilayers fabricated as stamping-assembly of CVD-grown monolayers. Bright domains in (a) correspond to H_h^h , whereas bright and dark domains in (b) correspond to R_h^M and R_h^X stackings. The insets show zooms to regions with nanoscopically reconstructed domains in hexagonal and triangular tilting. (c) Same but for a twisted H-type ($\delta = 179.7^\circ$) MoSe₂-WSe₂ heterobilayer. (d) and (e) Two regions of a twisted R-type ($\delta = 0.3^\circ$) MoSe₂-WSe₂ heterobilayer. All scale bars are 500 nm. The images were recorded at $\theta = 0^\circ$ and 38° for H- and R-type stacks, respectively, with a rotation angle $\phi = -20^\circ$ in (b), (d) and (e).

formation of diverse morphologies in stamping-assembled MoSe₂ homobilayers and MoSe₂-WSe₂ heterobilayers near parallel and antiparallel alignment. For CVD-grown WSe₂ homobilayers and WSe₂-MoSe₂ heterostructures, our imaging technique revealed complete reconstruction into domains of a single registry, with mutually exclusive R_h^M and R_h^X stacking configurations in R-type flakes and the tendency of R_h^M domain predominance. Our findings have immediate consequences for the optical properties of homobilayer [42] and heterobilayer stacks [11, 32] of semiconducting TMDs, and can be generalized to the entire class of van der Waals heterostructures with small lattice mismatch and twist angles.

METHODS

Sample fabrication: WSe₂ homobilayers as in Fig. 2 and Fig. 3 were synthesized by a one-step CVD growth as detailed in Ref. [42]. For the MoSe₂-MoSe₂ and MoSe₂-WSe₂ bilayers in Fig. 4, triangular single-crystal monolayers of MoSe₂ and WSe₂ were obtained separately from CVD synthesis. The

MoSe₂ layers were picked up with an adhesive polycarbonate stamp at a temperature of 145°C. The monolayer alignment to 0° (R-type) or 180° (H-type) was guided by straight triangle edges, with alignment precision limited to below 0.3°. The assembled stacks were successively released from the stamp onto a SiO₂/Si target substrate at a temperature of 180°C, then soaked in chloroform solution for 20 min to remove polycarbonate residues, cleaned by acetone and isopropanol and annealed at 200°C under ultrahigh vacuum for 12 hours. The WSe₂-MoSe₂ heterobilayers in Fig. 5 were grown by a two-step CVD process detailed in Ref. [32].

Secondary electron imaging: Secondary electron imaging was performed in a Raith-eLine SEM with an electron beam energy of 1.4 and 1.0 keV for H- and R-type stacks, respectively, at a working distance of 4.5 mm and an aperture of 30 μm. Carbon deposition during SEM-imaging [38, 39] was observed to reduce progressively the visibility of the registry-specific contrast. We note that the stacking nomenclature is relevant for the respective contrast in secondary electron

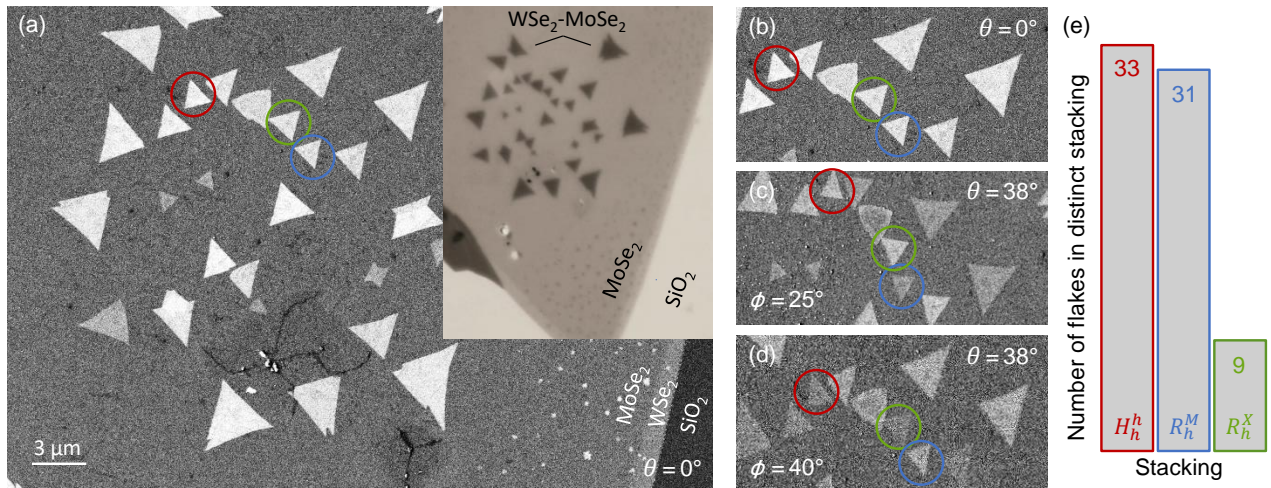


FIG. 5. (a) Secondary electron image at normal incidence ($\theta = 0^\circ$) and optical micrograph (top right inset) of CVD-grown WSe_2 - MoSe_2 heterostructures formed by a large bottom MoSe_2 monolayer and several WSe_2 triangular monolayers on top. Three representative triangles with different atomic registries are encircled in red, green and blue. (b), (c) and (d) Zooms to the region with the three triangles at normal incidence, and at $\phi = 25^\circ$ and 40° rotation for a tilt of $\theta = 38^\circ$. (e) Histogram count of different heterobilayer flakes with distinct atomic registries from several CVD-grown heterostacks. Note that due to reversed layer order of the CVD-grown heterostack the relative contrast of R-type registries is reversed.

imaging of heterobilayer registries. For the MoSe_2 - WSe_2 heterostructures studies in this work, the samples in Fig. 3(b) correspond to vertical stacks of bottom WSe_2 and top MoSe_2 monolayers, as shown schematically in Fig. 1(a) and (b) and used to introduce the registry nomenclature. The CVD-grown heterostack of Fig. 5, on the other hand, features the reversed layer order and thus opposite contrast behavior for a registry nomenclature with the subscript and superscript referring to the bottom and top layer, respectively. For stacks with bottom MoSe_2 and top WSe_2 monolayers, this implies that bright contrast at $\phi = 40^\circ$ corresponds to the R_h^M stacking.

Numerical simulations: Monte-Carlo simulations of the secondary electron yield as a function of tilt and rotation angle [27] were performed for all six registry configurations of a WSe_2 bilayer with lattice constant $a_0 = 3.28 \text{ \AA}$ and inter-layer distance $d = 6.60 \text{ \AA}$ [43] subjected to 49152 parallel incident electron trajectories per unit cell. We accounted for electron-electron interactions between the incident and bound electrons by a cylindrical cross-section of $r = 4a$ around each atom, with the nearest-neighbor interatomic distance $a = a_0/\sqrt{3}$. The scattering probability was calculated as $A(b/B)^{-2}$, where A specifies the secondary electron yield proportional to the number of covalently bound electrons, B is proportional to the covalent radius, and the impact parameter b is sensitive to the distance between the incoming electrons and the crystal atoms [27]. The constants A and B were determined from best-fits to experimental data with $A_{\text{Se}} = 0.09$, $A_{\text{W}} = 0.14$ and $B_{\text{Se}} = 0.3$, $B_{\text{W}} = 0.4$. The scattering probabilities were averaged over all trajectories at each ϕ for a given θ . Finally, the scattering probability was subtracted from unity to obtain the experimentally observed inverse secondary electron yield as discussed above (i.e. high secondary electron yield for the channelling case).

ACKNOWLEDGEMENTS

We thank P. Altpeter and C. Obermayer for assistance in the clean room. This research was funded by the European Research Council (ERC) under the Grant Agreement No. 772195 as well as the Deutsche Forschungsgemeinschaft (DFG, German Research Foundation) within the Priority Programme SPP 2244 2DMP and the Germany's Excellence Strategy EXC-2111-390814868 (MCQST). A. R. acknowledges funding by the Munich Quantum Valley doctoral fellowship program within the Bavarian initiative "Hightech Agenda Bayern Plus". A. S. B. received funding from the European Union's Framework Programme for Research and Innovation Horizon 2020 (2014–2020) under the Marie Skłodowska-Curie Grant Agreement No. 754388 (LMUResearchFellows) and from LMUexcellent, funded by the Federal Ministry of Education and Research (BMBF) and the Free State of Bavaria under the Excellence Strategy of the German Federal Government and the Länder. Z. L. was supported by the China Scholarship Council (CSC), No. 201808140196. S. Z. and I. B. acknowledge support from the Alexander von Humboldt Foundation.

REFERENCES

- [1] F. Wu, T. Lovorn, E. Tutuc, I. Martin, and A. MacDonald, Topological insulators in twisted transition metal dichalcogenide homobilayers, *Phys. Rev. Lett.* **122**, 086402 (2019).
- [2] L. Wang, E.-M. Shih, A. Ghiotto, L. Xian, D. A. Rhodes, C. Tan, M. Claassen, D. M. Kennes, Y. Bai, B. Kim, K. Watanabe, T. Taniguchi, X. Zhu, J. Hone, A. Rubio, A. N. Pasupathy, and C. R. Dean, Correlated electronic phases in twisted bilayer transition metal dichalcogenides, *Nat. Mater.* **19**, 861 (2020).
- [3] A. Ghiotto, E.-M. Shih, G. S. S. G. Pereira, D. A. Rhodes,

- B. Kim, J. Zang, A. J. Millis, K. Watanabe, T. Taniguchi, J. C. Hone, L. Wang, C. R. Dean, and A. N. Pasupathy, Quantum criticality in twisted transition metal dichalcogenides, *Nature* **597**, 345 (2021).
- [4] E. C. Regan, D. Wang, C. Jin, M. I. Bakti Utama, B. Gao, X. Wei, S. Zhao, W. Zhao, Z. Zhang, K. Yumigeta, *et al.*, Mott and generalized Wigner crystal states in WSe_2/WSe_2 moiré superlattices, *Nature* **579**, 359 (2020).
- [5] Y. Tang, L. Li, T. Li, Y. Xu, S. Liu, K. Barmak, K. Watanabe, T. Taniguchi, A. H. MacDonald, J. Shan, *et al.*, Simulation of Hubbard model physics in WSe_2/WSe_2 moiré superlattices, *Nature* **579**, 353 (2020).
- [6] Y. Xu, S. Liu, D. A. Rhodes, K. Watanabe, T. Taniguchi, J. Hone, V. Elser, K. F. Mak, and J. Shan, Correlated insulating states at fractional fillings of moiré superlattices, *Nature* **587**, 214 (2020).
- [7] X. Huang, T. Wang, S. Miao, C. Wang, Z. Li, Z. Lian, T. Taniguchi, K. Watanabe, S. Okamoto, D. Xiao, S.-F. Shi, and Y.-T. Cui, Correlated insulating states at fractional fillings of the WS_2/WSe_2 moiré lattice, *Nat. Phys.* **17**, 715 (2021).
- [8] H. Yu, G.-B. Liu, J. Tang, X. Xu, and W. Yao, Moiré excitons: From programmable quantum emitter arrays to spin-orbit-coupled artificial lattices, *Sci. Adv.* **3**, e1701696 (2017).
- [9] F. Wu, T. Lovorn, and A. H. MacDonald, Topological exciton bands in moiré heterojunctions, *Phys. Rev. Lett.* **118**, 147401 (2017).
- [10] N. Zhang, A. Surrente, M. Baranowski, D. K. Maude, P. Gant, A. Castellanos-Gomez, and P. Plochocka, Moiré intralayer excitons in a $MoSe_2/MoSe_2$ heterostructure, *Nano Lett.* **18**, 7651 (2018).
- [11] S. Zhao, Z. Li, X. Huang, A. Rupp, J. Göser, I. A. Vovk, S. Y. Kruchinin, K. Watanabe, T. Taniguchi, I. Bilgin, A. S. Baimuratov, and A. Högele, Excitons in mesoscopically reconstructed moiré heterostructures, *Nature Nanotechnology* 10.1038/s41565-023-01356-9 (2023).
- [12] F. Wu, T. Lovorn, and A. H. MacDonald, Theory of optical absorption by interlayer excitons in transition metal dichalcogenide heterobilayers, *Phys. Rev. B* **97**, 035306 (2018).
- [13] K. Tran, G. Moody, F. Wu, X. Lu, J. Choi, K. Kim, A. Rai, D. A. Sanchez, J. Qian, A. Singh, J. Embley, A. Zepeda, M. Campbell, T. Autry, T. Taniguchi, K. Watanabe, N. Lu, S. K. Banerjee, K. L. Silverman, S. Kim, E. Tutuc, L. Yang, A. H. MacDonald, and X. Li, Evidence for moiré excitons in van der Waals heterostructures, *Nature* **567**, 71 (2019).
- [14] C. Jin, E. C. Regan, A. Yan, M. Iqbal Bakti Utama, D. Wang, S. Zhao, Y. Qin, S. Yang, Z. Zheng, S. Shi, K. Watanabe, T. Taniguchi, S. Tongay, A. Zettl, and F. Wang, Observation of moiré excitons in WSe_2/WSe_2 heterostructure superlattices, *Nature* **567**, 76 (2019).
- [15] K. L. Seyler, P. Rivera, H. Yu, N. P. Wilson, E. L. Ray, D. G. Mandrus, J. Yan, W. Yao, and X. Xu, Signatures of moiré-trapped valley excitons in $MoSe_2/WSe_2$ heterobilayers, *Nature* **567**, 66 (2019).
- [16] M. Förg, A. S. Baimuratov, S. Y. Kruchinin, I. A. Vovk, J. Scherzer, J. Förste, V. Funk, K. Watanabe, T. Taniguchi, and A. Högele, Moiré excitons in $MoSe_2-WSe_2$ heterobilayers and heterotrayers, *Nat. Commun.* **12**, 1656 (2021).
- [17] E. M. Alexeev, D. A. Ruiz-Tijerina, M. Danovich, M. J. Hamer, D. J. Terry, P. K. Nayak, S. Ahn, S. Pak, J. Lee, J. I. Sohn, *et al.*, Resonantly hybridized excitons in moiré superlattices in van der Waals heterostructures, *Nature* **567**, 81 (2019).
- [18] W.-T. Hsu, B.-H. Lin, L.-S. Lu, M.-H. Lee, M.-W. Chu, L.-J. Li, W. Yao, W.-H. Chang, and C.-K. Shih, Tailoring excitonic states of van der Waals bilayers through stacking configuration, band alignment, and valley spin, *Sci. Adv.* **5**, eaax7407 (2019).
- [19] Y. Shimazaki, I. Schwartz, K. Watanabe, T. Taniguchi, M. Kroner, and A. Imamoğlu, Strongly correlated electrons and hybrid excitons in a moiré heterostructure, *Nature* **580**, 472 (2020).
- [20] S. Brem, K.-Q. Lin, R. Gillen, J. M. Bauer, J. Maultzsch, J. M. Lupton, and E. Malic, Hybridized intervalley moiré excitons and flat bands in twisted WSe_2 bilayers, *Nanoscale* **12**, 11088 (2020).
- [21] S. Carr, D. Massatt, S. B. Torrisi, P. Cazeaux, M. Luskin, and E. Kaxiras, Relaxation and domain formation in incommensurate two-dimensional heterostructures, *Phys. Rev. B* **98**, 224102 (2018).
- [22] M. R. Rosenberger, H.-J. Chuang, M. Phillips, V. P. Oleshko, K. M. McCreary, S. V. Sivaram, C. S. Hellberg, and B. T. Jonker, Twist angle-dependent atomic reconstruction and moiré patterns in transition metal dichalcogenide heterostructures, *ACS Nano* **14**, 4550 (2020).
- [23] V. Enaldiev, V. Zolyomi, C. Yelgel, S. Magorrian, and V. Fal'ko, Stacking domains and dislocation networks in marginally twisted bilayers of transition metal dichalcogenides, *Phys. Rev. Lett.* **124**, 206101 (2020).
- [24] A. Weston, Y. Zou, V. Enaldiev, A. Summerfield, N. Clark, V. Zolyomi, A. Graham, C. Yelgel, S. Magorrian, M. Zhou, J. Zultak, D. Hopkinson, A. Barinov, T. H. Bointon, A. Kretinin, N. R. Wilson, P. H. Beton, V. I. Fal'ko, S. J. Haigh, and R. Gorbachev, Atomic reconstruction in twisted bilayers of transition metal dichalcogenides, *Nat. Nanotechnol.* **15**, 592 (2020).
- [25] J. Sung, Y. Zhou, G. Scuri, V. Zolyomi, T. I. Andersen, H. Yoo, D. S. Wild, A. Y. Joe, R. J. Gelly, H. Heo, S. J. Magorrian, D. Bérubé, A. M. M. Valdivia, T. Taniguchi, K. Watanabe, M. D. Lukin, P. Kim, V. I. Fal'ko, and H. Park, Broken mirror symmetry in excitonic response of reconstructed domains in twisted $MoSe_2/MoSe_2$ bilayers, *Nat. Nanotechnol.* **15**, 750 (2020).
- [26] L. J. McGilly, A. Kerelsky, N. R. Finney, K. Shapovalov, E.-M. Shih, A. Ghiotto, Y. Zeng, S. L. Moore, W. Wu, Y. Bai, K. Watanabe, T. Taniguchi, M. Stengel, L. Zhou, J. Hone, X. Zhu, D. N. Basov, C. Dean, C. E. Dreyer, and A. N. Pasupathy, Visualization of moiré superlattices, *Nat. Nanotechnol.* **15**, 580 (2020).
- [27] T. I. Andersen, G. Scuri, A. Sushko, K. De Greve, J. Sung, Y. Zhou, D. S. Wild, R. J. Gelly, H. Heo, D. Bérubé, *et al.*, Excitons in a reconstructed moiré potential in twisted WSe_2/WSe_2 homobilayers, *Nat. Mater.* **20**, 480 (2021).
- [28] D. Halbertal, N. R. Finney, S. S. Sunku, A. Kerelsky, C. Rubio-Verdú, S. Shabani, L. Xian, S. Carr, S. Chen, C. Zhang, L. Wang, D. Gonzalez-Acevedo, A. S. McLeod, D. Rhodes, K. Watanabe, T. Taniguchi, E. Kaxiras, C. R. Dean, J. C. Hone, A. N. Pasupathy, D. M. Kennes, A. Rubio, and D. N. Basov, Moiré metrology of energy landscapes in van der Waals heterostructures, *Nat. Commun.* **12**, 242 (2021).
- [29] S. Shabani, D. Halbertal, W. Wu, M. Chen, S. Liu, J. Hone, W. Yao, D. N. Basov, X. Zhu, and A. N. Pasupathy, Deep moiré potentials in twisted transition metal dichalcogenide bilayers, *Nat. Phys.* **17**, 720 (2021).
- [30] V. V. Enaldiev, F. Ferreira, S. J. Magorrian, and V. I. Fal'ko, Piezoelectric networks and ferroelectric domains in twistrionic superlattices in $WS_2/MoSe_2$ and $WSe_2/MoSe_2$ bilayers, *2D Mater.* **8**, 025030 (2021).
- [31] A. Weston, E. G. Castanon, V. Enaldiev, F. Ferreira, S. Bhattacherjee, S. Xu, H. Corte-León, Z. Wu, N. Clark, A. Summerfield, T. Hashimoto, Y. Gao, W. Wang, M. Hamer, H. Read, L. Fumagalli, A. V. Kretinin, S. J. Haigh, O. Kazakova, A. K. Geim, V. I. Fal'ko, and R. Gorbachev, Interfacial ferroelectric-

- ity in marginally twisted 2D semiconductors, *Nat. Nanotechnol.* **17**, 390 (2022).
- [32] Z. Li, F. Tabataba-Vakili, S. Zhao, A. Rupp, I. Bilgin, Z. Herdgen, B. März, K. Watanabe, T. Taniguchi, G. R. Schleder, A. S. Baimuratov, E. Kaxiras, K. Müller-Caspary, and A. Högele, Lattice reconstruction in MoSe₂-WSe₂ heterobilayers synthesized by chemical vapor deposition, *Nano Lett.* **23**, 4160 (2023).
- [33] J. S. Alden, A. W. Tsen, P. Y. Huang, R. Hovden, L. Brown, J. Park, D. A. Muller, and P. L. McEuen, Strain solitons and topological defects in bilayer graphene, *Proc. Natl. Acad. Sci.* **110**, 11256 (2013).
- [34] A. Rupp, J. Göser, Z. Li, P. Altpeter, I. Bilgin, and A. Högele, Energy-dispersive x-ray spectroscopy of atomically thin semiconductors and heterostructures, *Phys. Rev. Appl.* **18**, 064061 (2022).
- [35] K. Ashida, T. Kajino, Y. Kutsuma, N. Ohtani, and T. Kaneko, Crystallographic orientation dependence of SEM contrast revealed by SiC polytypes, *J. Vac. Sci. Technol. B* **33**, 04E104 (2015).
- [36] K. Hermann, Periodic overlays and moiré patterns: theoretical studies of geometric properties, *J. Phys. Condens. Mat.* **24**, 314210 (2012).
- [37] H. Baek, M. Brotons-Gisbert, Z. X. Koong, A. Campbell, M. Rambach, K. Watanabe, T. Taniguchi, and B. D. Gerardot, Highly energy-tunable quantum light from moiré-trapped excitons, *Sci. Adv.* **6**, eaba8526 (2020).
- [38] L. Reimer, *Scanning electron microscopy: physics of image formation and microanalysis* (Springer, 1984).
- [39] J. I. Goldstein, D. E. Newbury, J. R. Michael, N. W. Ritchie, J. H. J. Scott, and D. C. Joy, *Scanning electron microscopy and X-ray microanalysis* (Springer, 2017).
- [40] D. C. Joy, D. E. Newbury, and D. L. Davidson, Electron channeling patterns in the scanning electron microscope, *J. Appl. Phys.* **53**, R81 (1982).
- [41] D. Purdie, N. Pugno, T. Taniguchi, K. Watanabe, A. Ferrari, and A. Lombardo, Cleaning interfaces in layered materials heterostructures, *Nat. Commun.* **9**, 5387 (2018).
- [42] Z. Li, J. Förste, K. Watanabe, T. Taniguchi, B. Urbaszek, A. S. Baimuratov, I. C. Gerber, A. Högele, and I. Bilgin, Stacking-dependent exciton multiplicity in WSe₂ bilayers, *Phys. Rev. B* **106**, 045411 (2022).
- [43] J. He, K. Hummer, and C. Franchini, Stacking effects on the electronic and optical properties of bilayer transition metal dichalcogenides MoS₂, MoSe₂, WS₂, and WSe₂, *Phys. Rev. B* **89**, 075409 (2014).